An integrated and homogenized global surface solar radiation dataset and its reconstruction based on a convolutional neural network approach

Boyang Jiao[1,#], Yucheng Su[2], Qingxiang Li*[1,#], Veronica Manara[3],Martin Wild[4]

[1]School of Atmospheric Sciences, Sun Yat-sen University, and Key Laboratory of Tropical Atmosphere−Ocean System, Ministry of Education, Zhuhai 519082, China

[2]Meteorological Bureau of Zhuhai, Zhuhai 519082, China

[3]Department of Environmental Science and Policy, Università degli Studi di Milano, via Celoria 10, 20133, Milano, Italy

[4]Institute for Atmospheric and Climate Science, ETH Zurich, Zurich, Switzerland

[#]Southern Laboratory of Ocean Science and Engineering (Guangdong Zhuhai), Zhuhai 519082, China

Correspondence to: Qingxiang Li (liqingx5@mail.sysu.edu.cn)

Abstract

Surface solar radiation (SSR) is an essential factor in the flow of surface energy, enabling accurate capturing of long-term climate change and understanding the energy balance of Earth's atmosphere system. However, the long-term trend estimation of SSR is subjected to significant uncertainties due to the temporal inhomogeneity and the uneven spatial distribution of the *in situ* observations. This paper develops an observational integrated and homogenized global-terrestrial (except for Antarctica)) stational SSR dataset (SSRIH$_{station}$) by integrating all available SSR observations, including the existing homogenized SSR results. The series is then interpolated in order to obtain a 5°×5° resolution gridded dataset (SSRIH$_{grid}$). On this basis, we further reconstruct a long-term (1955-2018) global land (except for Antarctica) SSR anomalies dataset with a 5°×2.5° resolution (SSRIH$_{20CR}$) by training improved partial convolutional neural network deep learning methods based on the reanalysis 20CRv3. Based on this, we analysed the global land (except for Antarctica) /regional scale SSR trends and spatiotemporal variations: The reconstruction results reflect the distribution of SSR anomalies and have high reliability in filling and reconstructing the missing values. At the global land (except for Antarctica) scale, the decreasing trend of the SSRIH$_{20CR}$ (-1.276 ± 0.205 W/m^2 per decade) is smaller than the trend of the SSRIH$_{grid}$ (-1.776 ± 0.230 W/m^2 per decade) from 1955 to 1991. The trend of SSRIH$_{20CR}$ (0.697 ± 0.359 W/m^2 per decade) from 1991 to 2018 is also marginally lower than that of the SSRIH$_{grid}$ (0.851 ± 0.410 W/m^2 per decade). At the regional scale, the difference between the SSRIH$_{20CR}$ and SSRIH$_{grid}$ is more significant in years and areas with insufficient coverage. Asia, Africa, Europe and North America cause the global dimming of the SSRIH$_{20CR}$, while Europe and North America drive the global brightening of the SSRIH$_{20CR}$. Spatial sampling inadequacies have largely contributed to a bias in the long-term variation of global /regional SSR. This paper's homogenized gridded dataset and the Artificial Intelligence reconstruction gridded dataset (Jiao and Li, 2023) are all available at https://doi.org/10.6084/m9.figshare.21625079.v1.

1 Introduction

Energy flows at the Earth's surface play an essential role in climate change and human activity and link to physical processes such as global warming, glacier retreating, hydrological cycle, and carbon budget (Hoskins and Valdes, 1990; Peixoto et al., 1992; Trenberth and Fasullo, 2013; Wild, 2012). As a critical factor characterizing surface energy flows, Surface Solar Radiation (SSR) largely determines the climatic conditions and ecological environment in which we live. Therefore, a more accurate and comprehensive analysis of the SSR fluxes will help better understand the Earth's atmospheric system. *In situ* observations provide the most accurate baseline data for measuring SSR. They allowed for the first time the detection of decadal changes in SSR known as "dimming and brightening" (Wild et al., 2005), especially considering that they cover a longer period concerning another type of data like for example satellite data (Pfeifroth et al., 2018). Even observational data often have uneven distribution and missing data with respect to the satellite data, especially in areas with complex orography (Manara et al., 2020).

The sources of *in situ* SSR observations are mainly collected from the Global Energy Balance Archive (GEBA) (Wild et al., 2017) and the World Radiation Data Centre (WRDC) (Tsvetkov et al., 1995). Furthermore, other SSR station series are obtained from the high quality Baseline Surface Radiation Network (BSRN) (Driemel et al., 2018) and the data centres of individual national hydrometeorological services. However, two issues still need to be addressed: 1) the inhomogeneity of station data resulting from station relocations and instrumentation changes severely impacts the climate change assessment. For the regions with a relatively high density of stations, like Europe (Manara et al., 2019; Manara et al., 2016; Sanchez-Lorenzo et al., 2013a; Sanchez-Lorenzo et al., 2015; Sanchez-Lorenzo et al., 2013b), Japan (Ma et al., 2022) and China (Ju et al., 2006; Wang, 2014; Wang et al., 2015; Wang and Wild, 2016; Yang et al., 2018b; You et al., 2013), much previous work has redefined the degree and timing of "dimming and brightening" by addressing the inhomogeneity of the SSR data series. For example, in Spain, the average annual homogenized SSR series has a significant increasing trend (+ 3.9 W/m^2 per decade) during the 1985–2010 period (Sanchez-Lorenzo et al., 2013a). The period of dimming observed in Italy's homogenized SSR series is not apparent in the 1960s and early 1970s when the raw series (inhomogenized) are taken into account (Manara et al., 2016). The direct measurements of SSR show a level trend from 1961 to 2014 over Japan, while their homogenization series display a decreasing trend (0.8-1.6 W/m^2 per decade) (Ma et al., 2022). In China, homogenization largely eliminated the dramatic

69   non-climatic rise of the early 1990s and also reduced the increasing trend from 1990 to 2016 (Yang et

70   al., 2018b). However, most of the research was still limited to regional scales. 2) The issue of limited

71   spatial sampling of long observational stations and their uneven distribution especially over areas with

72   complex orography. Considerable efforts have been devoted to filling in /interpolating the missing values

73   in climate datasets ("spatial analysis") (Collins, 1996; Erxleben et al., 2002; Scudiero et al., 2016). The

74   traditional spatial interpolation methods commonly used include Inverse Distance Weighted (Fisher et

75   al., 1993; Shepard, 1968), Kriging (Krige, 1951), Thin-Plate Splines (Bookstein, 1989) et cetera. Since

76   the 1980s, physical parametric interpolation (Feng and Wang, 2021; Tang et al., 2019) and Bayesian

77   fusion schemes (Aguiar et al., 2015) based on multi-source observational data were widely used, when

78   the emergence of highly accurate and relatively precise satellite data. However, the resulting fusion

79   datasets cover a too short period to investigate their decadal and multi-decadal variations and to study

80   the underlying causes. The spatial, temporal, and spectral coverage of a single satellite is limited, and

81   multiple satellite data are therefore often used in tandem with each other; however, such a

82   discontinuity in time and space can introduce inhomogeneity into a dataset (Evan et al., 2007; Feng

83   and Wang, 2021; Shao et al., 2022). Reanalysis products are an important complement containing

84   long-term SSR data, therefore have been widely used in climate studies (Huang et al., 2018; Jiao et

85   al., 2022; Urraca et al., 2018; Zhou et al., 2018a; Zhou et al., 2017) due to the dynamically consistent

86   and spatiotemporally complete atmospheric fields with high resolution and open access to data.

87   However, existing studies have shown that reanalysis products generally overestimate multi-year

88   mean SSR values compared to observations over land (He et al., 2021). With the continuous

89   development of climate system simulations, model data from the Coupled Model International

90   Program (CMIP) have become an important resource for conducting climate change research (Gates

91   et al., 1999; Zhou et al., 2019). Previous studies have shown that the models used in CMIP6

92   overestimate the global mean SSR (He et al., 2023; Jiao et al., 2022; Wild, 2020). The rise of deep

93   learning and big data techniques has brought about an explosion of artificial intelligence (AI). Machine

94   learning is increasingly being used in spatial interpolation, such as the spatial reconstruction of surface

95   temperature datasets (Huang et al., 2022; Kadow et al., 2020; Cao et al., 2022), the spatial and temporal

96   reconstruction of turbulence resolution (Fukami et al., 2021), etc. Furthermore, it shows high accuracy

97   and low uncertainty in reproducing and predicting SSR (Leirvik and Yuan, 2021; Tang et al., 2016; Yang

98   et al., 2018a; Yuan et al., 2021). However, long-term homogenized SSR datasets with global terrestrial

99   coverage have yet to be developed, resulting in significant uncertainties in assessing global SSR variation

100   (Jiao et al., 2022).

101   Therefore, developing a more homogeneous and comprehensive global long-term SSR climatic dataset

102   that provides a better benchmark for observational constraints on the global surface energy balance

103   /budget remains a valuable and challenging task. This paper first homogenizes and grids the most

104   extensive collection of available global SSR station observations. Then, the missing grid boxes /years

105   are spatially interpolated using a convolutional neural network (CNN) approach to obtain a globally

106   covered land surface SSR anomalies dataset. Finally, the reconstructed datasets are initially analysed and

107   evaluated. Thus, the paper is divided into seven main sections. The data resources are introduced in

108   Section 2. Section 3 presents the data homogenization, and the CNN model reconstruction methods. The

109   data homogenization and verification are shown in Section 4. Section 5 gives the AI reconstruction results.

110   Section 6 is the availability of the datasets. Conclusions are provided at the end of the paper.

111   **2 Data**

112   Nine SSR datasets are collected to derive the global SSR variable. In particular, six datasets contain data

113   from observational stations (Section 2.1): two global ground-based measurement datasets (GEBA,

114   WRDC) and four homogenized products at regional and country levels (Europe, China, Japan and Italy).

115   Three of the adopted datasets are reanalysis data (Section 2.2.1): Fifth generation European Centre for

116   Medium-Range Weather Forecasts (ECMWF) reanalysis (ERA5), 20th Century Reanalysis version 3

117   (20CRv3) reanalysis data and the Coupled Model Intercomparison Project Phase 6 (CMIP6) historical

118   simulation output (125). Specifically, the ERA5 data are used to fill the data over oceans and Antarctica

119   (Section 3.2.1), 20CRv3 data and CMIP6 simulations are used for the AI model training (Section 5.1)

120   and reconstruction. All have been listed in Table 1.

121   **2.1 In situ observational Data**

122   **2.1.1 Global datasets**

123   There are two main sources of raw SSR data (see Table 1): the ETH Zurich GEBA with monthly data

124   from 2,445 globally distributed stations, starting from 1922 until 2020, and the WRDC dataset with

125   monthly globally distributed data from 1136 stations since 1964. The first one is available for download

at https://geba.ethz.ch (Last access: 2022.7. 2). The second one published the first SSR radiation balance data in 1965 and then its publication has been issued four times a year since 1993 and is available for download at http://wrdc.mgo.rssi.ru/ (Last access: July 2021).

2.1.2 National (regional) homogenized station datasets

1) Chinese homogenized SSR dataset

The China Meteorological Radiation Fundamental Elements Monthly Value Data Set has been downloaded at http://www.nmic.cn. The homogenized SSR dataset in China is released by the National Meteorological Information Centre (NMIC), China Meteorological Administration (CMA) (Yang, 2016). The data are available for the period between Jan 1950 to Dec 2014, and the follow-up data are extended with raw observations from NMIC. They used the sunshine duration (SSD) data from nearby stations to construct an arguably better reference to identify inhomogeneities in the SSR data. Then, a combined metadata and the maximum penalty t-test (PMT) method was used to detect the change points. Finally, they were adjusted by a quantile matching (QM) algorithm (Wang and Feng, 2013). The final homogenized SSR station dataset was converted to gridded data using the first difference method (FDM (Peterson et al., 1998)) and is available for download at http://www.nmic.cn. Last Access: September 2022.

2) Japanese homogenized SSR dataset

Ma et al. (Ma et al., 2022) released a Japanese SSR homogenized dataset in 2022 spanning the period between 1870 and 2015. First, they homogenized SSD based on PMF (penalized maximal F test) and QM algorithms. They then used the homogenized SSD from the previous step as a reference series, combined with metadata and PMT, to detect change points. Finally, they adjusted the change points by the QM algorithm. For more details on data descriptions, the adopted methodology and downloading data refer to https://data.tpdc.ac.cn/en/data/45d73756-3f5a-4d27-82a4-952e268c20e8/, Last Access: March 2022.

3) European homogenized SSR data

A homogenized dataset of European SSR stations was developed by Sanchez-Lorenzo et al. (Sanchez-Lorenzo et al., 2015) and is currently available as a full public download at https://agupubs.onlinelibrary.wiley.com/doi/full/10.1002/2015JD023321. They selected the 56 longest Central European SSR series available in GEBA dataset with data for the period comprised between

155 1922 and 2012. They adjusted them to ensure temporal homogeneity homogenizing the data with the

156 Standard Normal Homogeneity Test (Alexandersson, 1986) and the Craddock test (Craddock, 1979).

157 4) Italian homogenized SSR dataset

158 The Italian homogenized SSR datasets are those published by (Manara et al., 2019; Manara et al.,

159 2016). As candidate stations to use as reference series, they selected the ten series located in the same

160 area of the series to be tested and that series correlate well with the test one. In particular, they tested the

161 change points with the Craddock test (Manara. et al., 2017) and when a break is identified by more than

162 one reference series the preceding portion of the series is corrected, leaving the most recent portion

163 unchanged. In this way, the SSR stations were homogenized, and then the missing values were

164 interpolated.

165 **2.2 Other datasets**

166 **2.2.1 Reanalysis**

167 ERA5 can be used to fill in SSR data from the oceans and Antarctica and carry out the global

168 reconstruction, taking into account its high spatial resolution and reliable performance of SSR (Jiao et

169 al., 2022; Liang et al., 2022). After the reconstruction, we removed the data for the ocean reanalysis and

170 maintain the data only in the land area (except for Antarctica). In addition, two SSR data products

171 (20CRv3, CMIP6) are used to train AI models. These are:

172 1) ERA5 (space-filling data): ERA5 is the fifth generation of the European Centre for Medium-Range

173 Forecasting reanalysis product, which currently publishes data from 1950 to the present (Hersbach et al.,

174 2020). In addition, ERA5 has an hourly output and an uncertainty estimate from the ensemble. The data

175 is based on the Integrated Forecasting Model Cy41r2 run in 2016, which contains a 4D-Var assimilation

176 scheme. In ERA5, SSR is obtained from a Rapid Radiation Transfer Model (RRTM) (Mlawer et al.,

177 1997). The present study utilizes monthly SSR data for the period 1955-2018 from ERA5 with a

178 resolution of $0.25° \times 0.25°$ (last accessed in July 2022). It can be downloaded at

179 https://cds.climate.copernicus.eu

180 2) 20CRv3 (data for AI model training): The 20CR Project is an effort led by NOAA's Physical

181 Sciences Laboratory and CIRES at the University of Colorado, supported by the Department of Energy,

182 to produce reanalysis datasets spanning the entire 20th century and much of the 19th century (Slivinski

183 et al., 2019). 20CR provides a comprehensive global atmospheric circulation data set from 1850 to 2015.

184   Its chief motivation is to provide an observational validation dataset, with quantified uncertainties, for

185   assessing climate model simulations of the 20th century. 20CR uses an ensemble filter data assimilation

186   method which directly estimates the most likely state of the global atmosphere every three hours and

187   estimates the uncertainty in that analysis. The most recent version of this reanalysis, 20CRv3, provides

188   8-times daily estimates of global tropospheric variability across 75 km grids, spanning 1836 to 2015

189   (with an experimental extension from 1806 to 1835). The present study uses monthly SSR data of

190   20CRv3 (NOAA /CIRES /DOE 20CR, 80 members) from 1955-2015. We selected all 80 members of

191   the 20CR as input (1 for evaluation and to test reconstruction, the other 79 for training the CNN model).

192   The SSR of 20CRv3 has a spatial resolution of 0.7°×0.7° (Last accessed: May 2022). The download is

193   available at https://portal.nersc.gov/archive/home/projects/incite11/.

194   **2.2.2 CMIP6 models output**

195   3) CMIP6 models output (data for AI model training): the Coupled Model Intercomparison Project,

196   driven by the World Climate Research Program, is now in its 6th phase. Specifically, CMIP6 is

197   considered as the current state of the art way of producing future climate simulations, including predicting

198   future SSR based on different climate scenarios (Zhou et al., 2018b). It provides an important resource

199   for studying current and future climate change (Eyring et al., 2016). The historical simulations of CMIP6

200   are designed to reproduce observed climate and climate change, constrained by radiative forcing. Its

201   historical simulation spans between 1850 and 2014. In this study, we selected 125 members out of a total

202   of 507 members from several CMIP6 large ensemble models (with more than 10 realizations/runs) with

203   high correlation coefficients with observations as input to train and validate the CNN model (1 for

204   evaluation and to test reconstruction, the other 124 for training the CNN model). We selected the monthly

205   downward shortwave radiation from 1955 to 2014 (see Table S1 in the Supplemental Material (SM)).

206   Last access July 2022. Download at: https://esgf-node.llnl.gov/search/cmip6.

3 Methods

3.1 Data Quality Control (QC) and homogenization

The SSR data homogenization method is only applied to the two inhomogenized *in situ* observations datasets (GEBA and WRDC). The Quality Control (QC) and homogenization flowchart (Figure 1) is divided into three steps: 1. QC; 2. Homogenization; 3. Integration and consolidation.

3.1.1 QC

The QC of SSR data includes the following steps:

1) Simple integration: integration of the GEBA (2445) and WRDC (1136) datasets removing stations with no data and leaving 2681 stations.

2) Removing duplicate stations: a. Stations with similar latitude and longitude. We consider two stations with totally identical latitude and longitude to be the same station; b. Stations less than 10km apart. We averaged the duplicate stations in this a and b case; c. Special duplicate stations: Stitching together data of the duplicate stations based on metadata from CMA.

3) Remove stations or years /months for which a climatic analysis cannot be established: we remove stations with records of less than ten years and values more than three times (3σ criterion (Olanow and Koller, 1998) the standard deviation of the SSR anomalies.

4) Candidate stations (487) with a record length greater than 15 years in the period 1971-2000 are selected. We added stations (715) with more than 10 years of SSR records to increase the number of available stations for a better homogenization of the candidate stations (Figure 2).

3.1.2 Station series homogenization

This paper uses the RHtestV4 software package to test and adjust the SSR station data for homogeneity (http://etccdi.pacificclimate.org/software.shtml) (Wang and Feng, 2013). The package is based on the empirical penalty functions PMF (Wang, 2008a) and PMT (Wang, 2008b; Wang et al., 2007) for the homogenization test. It takes into account the lag-1 autocorrelation of the time series. It embeds a multiple linear regression algorithm to significantly reduce the problem of an unbalanced distribution of pseudo-identification rates and test efficacy. Also, RHtestV4 uses the QM algorithm (Vincent et al., 2012; Wang et al., 2010) and Mean-Adjustments to adjust the identified change points.

The specific steps are as follows:

235   1) Building the reference series

236   a. We processed the data from all stations series (715) into the annual first differences (FD) series

237   e_i(Eq. (1)) (Peterson et al., 1998).

238   b. We calculated the correlation of the annual FD series between the series from the potential reference

239   pool and the candidate stations.

240   c. We calculated the distance between the potential reference pool stations and candidate stations.

241   d. We selected potential stations according to the correlation coefficient (CC >= 0.6) between the series

242   from potential reference pool and candidate stations. And the potential stations also satisfy the limits in

243   distances (<= 500km) between the potential pool stations and candidate stations.

244   e. We obtain the reference FD series (Re)based on the m potential reference series (Pe$_i$) and the CCs

245   (c_i) between the potential reference series (Pe$_i$) and candidate stations series (Eq. (2)).

246   f. The synthesized reference FD series (Re) (Eq. (2)), plus the average of all potential reference series

247   ($\bar{R}$), yields the final annual reference series (R) (Eq. (3)).

$$e_i = x_i - x_{i+1}$$

$$i=1, 2, \ldots, n-1 \qquad (1)$$

$$R_e = \frac{\sum_{i=1}^{m} Pe_i * c_i^2}{\sum_{i=1}^{m} c_i^2} \qquad (2)$$

$$R = R_e + \overline{R} \qquad (3)$$

248   e_i Annual FD series,

249   x_i Raw observational station SSR in the year i,

250   Re Final reference series,

251   Pe_i Potential reference series,

252   c_i CC between the potential reference series and the candidate stations series.

253   2) Testing and adjusting the candidate series

254   The homogenization test algorithm used in this paper is the PMT. This method is a reference series-

255   dependent test for a normalized candidate series. It assumes that the linear trend of the time series is zero

256   and uses the degree of mean deviation at different points in the series to find change points. Furthermore,

257   it eliminates the effect of different sample lengths on the test results. At the same time, the method

258   introduces an empirical penalty factor, which effectively improves detection. We used the PMT to test

259   the homogeneity of the candidate series based on the reference series established in 1). We then adjusted

260   the statistically significant(p>0.05) changepoints obtained using the mean adjustment method (p>0.05).

261   We homogenize the monthly series for 66 stations (see Figure S1 in the SM).

3.1.3 Integration and consolidation

263   As can be seen from Figure 1, the candidate stations (487) are relatively sparse. To better adapt deep

264   learning methods for the dataset reconstruction later, we adjusted, added and integrated station series

265   based on the results of homogenized data from other scholars: 1) We added stations with more than 10a

266   overall (1955-2018) records but no more than 15a during the 1971-2000 period, and removed those

267   stations that were clearly inhomogeneous (25) and some years of the station (3); 2) We subsequently

268   integrate monthly SSR series for 116 stations based on the results of homogenization by other scholars

269   (China (56), Japan (8), Europe (2) and Italy (50)). After the above steps, we end up with a homogenized

270   dataset containing 944 stations (Figure 3). The details of the processing and classification are shown in

271   Table S2 (see in the SM).

3.2 CNN model reconstruction methods

273   The CNN deep learning model network architecture uses a U-shaped structure similar to the U-net

274   (Ronneberger et al., 2015). The advantage of using this model is: 1) both high and low-frequency

275   information of the picture can be retained, and when reconstructing the SSR data, not only the grid point

276   information close to the missing measurement point will be considered, but also information from more

277   distant locations (which may be remotely correlated with that missing measurement point); 2) This makes

278   the model convergence faster and more economical in terms of computational resources. The upper part

279   of the U-shaped structure, which has no down samples or a low number of down samples, represents the

280   high-frequency information of the graph. These sections contain much of the detail in the graph and the

281   relationships between similar grid points are conveyed by this section. The lower half of the U-shaped

282   structure is down-sampled more often and represents the lower frequency information of the graph. The

283   global radiation of a wide range of undulations is transmitted by it, and then the information at the various

284   levels of the U-shaped structure is connected and transmitted through the skip connection, allowing the

285   whole network to remember all the information of the picture very well. The model uses nearest

286   neighbour upsampling in the decoding phase, the skip links will concatenate two feature maps and two

287   masks as the feature and mask inputs for the next part of the convolution layer. The input to the last part

288 of the convolution layer will contain the original input image concatenated with the holes and the original

289 mask, allowing the model to replicate the gap-free pixels. The complex and variable nature of the sea-

290 land boundary then has a significant impact on the reconstruction, when we reconstruct the global land

291 SSR data. Therefore, we use partial convolution at the image boundaries with a suitable image padding,

292 ensuring that the padding content at the image boundaries is not affected by values outside the image.

293 The deep learning models' convolutional layers and loss functions have been described in the SM.

294   We further reconstruct a long-term (1955-2018) global SSR anomalies dataset (SSRIH$_{20CR}$) by using

295 improved partial CNN deep learning methods based on a "perfect" dataset. CNN consists of three parts.

296 A convolutional layer to reduce the number of weights by extracting local features, a pooling layer to

297 reduce peacekeeping and prevent overfitting, and a fully connected layer to output the desired result. In

298 this paper, a modified CNN network is used to model the reconstruction of the SSR data, with the

299 convolutional layer replaced by a partial convolution method and mask update. This method is the latest

300 in image restoration effects and can restore irregular holes, an advantage over other image restoration

301 methods that can only restore rectangular holes. Therefore, this paper uses the modified CNN model

302 (Kadow et al., 2020) to recover the missing part of the global terrestrial SSR (except Antarctica). The

303 specific reconstruction steps and processes are as in Figure 4.

304 **3.2.1 Data pre-processing**

305 The homogenized station data is converted to grid box anomalies using the Climate Anomalies Method

306 (CAM) (Jones et al., 2001). CAM is a commonly used method for converting station anomaly data to

307 gridded data. We divide all global areas into a $5° \times 5°$ grid, after which we calculate the SSR anomalies

308 (relative to 1923-2020) within the grid box by averaging the anomalies of all stations (at least 1 station

309 in it). If there are more than one site exists in the same grid box, the record length of this grid box is the

310 total length of all sites in that grid box. Finally, we removed the values that were more than three times

311 the standard deviation of the SSR anomaly time series after gridding. SSRs are all processed as daily

312 average anomalies, i.e., monthly anomalies divided by 30 (each month is approximated as 30 days). We

313 multiplied all the values by 30 again when the reconstruction is complete. The global land (except for

314 Antarctica) distribution and coverage of SSRs after gridding are shown in Figure 5 a, b.

315   As seen in Figure 5a, the SSR is spatially sparsely distributed across South America and Africa. As

316 shown in Figure 5b, SSR coverage increased yearly from 1950 until the mid-1970s, when it slowly

317 decreased. In 2013, the coverage rate decreased sharply due to untimely data submission. Considering

318 the SSR coverage above, we only kept the years (1955-2018) with data coverage of more than 8% of

319 global land (except for Antarctica) areas.

320 Comparisons show that the ERA5 has high spatial resolution and relatively reliable performance in

321 the temporal variations and long-term trends (Liang et al., 2022; Jiao et al., 2022). To obtain a higher

322 data coverage and ensure that the AI model runs well, we used the ERA5 to fill the SSR of homogenized

323 global gridded SSR in the Antarctic and ocean areas. However, if we use the SSR of ERA5 to directly

324 fill the SSR of homogenized global gridded SSR (SSRIH$_{grid}$) in the Antarctic and on the ocean areas,

325 then the relatively weaker ocean SSR variations (variabilities, decadal changes, trends, etc.) from ERA5

326 will inevitably introduce certain systematic biases in land SSR reconstruction due to the SSRs have the

327 lower coverage on the land. Therefore, we designed an algorithm to avoid excessive diffusion of SSR

328 system bias in terrestrial areas: we first calculated the ratios $\gamma_i(i=1, 2, 3, ..., n)$ between the SSR from

329 ERA5 and from SSRIH$_{grid}$ on the land in all n years. For a single grid box, the γ_i have small changes

330 and are regarded as a constant γ_{median} (Eq (4)), and the γ_{median} vary by latitude and longitude both on

331 the marine and the land areas. We then extrapolated the γ_{median} for all the grid boxes along the land

332 and sea boundaries. If there is no observation there, then the adjacent ocean ERA5 SSR is used to take

333 its place after it is adjusted according to the differences between the SSR variations (represented by the

334 linear trends) for the different underlying surfaces (Eq (5).

$$\gamma_{median} = Median(\frac{OBS_{i\_land}}{ERA5_{i\_land}}), \qquad (4)$$

$$OBS_{i\_O\&L}(land) = ERA5_{i\_O\&L}(Ocean) * \gamma_{median} * \frac{T_O}{T_L}, \qquad (5)$$

$$i = 1,2,3......, n$$

335 γ_{median}: The median value of the ratios of OBS and ERA5 land SSR series,

336 OBS_{i_land}: Land SSR for the year i from SSRIH$_{grid}$ in a single grid,

337 $ERA5_{i\_land}$: Land SSR for the year i from ERA5in a single grid,

338 $OBS_{i\_O\&L}(land)$: LandSSRalong the sea-land boundary(land) for the year i from SSRIH$_{grid}$,

339 $ERA5_{i\_O\&L}(Ocean)$: Ocean SSR along the sea-land boundaryfor the year i from ERA5,

340 T_O: Trend of ERA5 SSR on ocean areasin all n years,

341 T_l: Trend of ERA5 SSR on areas in all n years.

3.2.2 AI Model reconstruction

We use a server (configured with processor Intel (R) Core (TM) i7-8700 CPU @ 3.20GHz 3.19 GHz, RAM 32G, 64-bit OS, GPU model 516.94, NVIDIA GeForce 1080T version, Python 3.9.12 64-bit, CUDA 10.1) for AI models training. The specific training steps are as follows:

  1) A total of 768 missing value masks (monthly masks between 1955 and 2018) were prepared for training and validation using '1' for existing and '0' for missing values;

  2) The 20CRv3 /CMIP6 training set (monthly values between 1955 and 2015 /2014) and missing value masks are fed into the 20CR-AI /CMIP6-AI model for training;

  3) We perform 1,500,000 training sessions with an interval of 10,000 sessions for the training output model.

  Afterwards, the two AI models are validated against the root mean squared error (RMSE) /CCs of the reconstructed SSRs (SSR_{20CR}/SSR_{CMIP6}). The validation set SSRs, and the optimal number of training cycles is 1,100,000 (see Figure S2, Figure S3 and Figure S4 in the SM). The initial hyper-parameters of the model are set as follows; learning rate of 2e-4 and learning finetune of 5e-5. First, we set the batch size to 16 in the first 500000 iterations and fine-tuned it to 18 in the last 10000000 iterations, for a total of 1500000 iterations, to suppress the overfitting phenomenon generated during the training process, and validate the model every 10000 times and early stopping if the validation shows a decreasing trend, the final number of training times used is 1100000. Second, L2 regularization is also added to regulate the loss function (see Eq. (9) in the SM).

  The training result models generated by the different AI models are obtained separately for the different training sets. The model is first used to reconstruct a reanalysis validation set with the same missing value mask as the original observation dataset. This is followed by a validation of the reconstruction against the original reanalysis dataset (calculation of CC and RMSE) to understand the discrepancies in the model reconstruction.

4 Data homogenization and verification

We homogenized the original monthly stations /gridded SSR time series ($SSRIH_{station}$ /$SSRIH_{grid}$) using the method in section 3.1.2. We selected six continental regions, excluding Antarctica and the Arctic, from the eight continents of the world defined by Xu et al. (Xu et al., 2018) (Asia, Africa, South America,

370   Europe, North America, Australia, Antarctica and the Arctic). The decreasing trend of the SSRIH$_{grid}$ is

371   consistent with the original gridded SSR series (SSRI$_{grid}$) during 1955-1991 while the increasing trend

372   during 1991-2018 is weaker. At the regional scale, the SSRIH$_{grid}$ has a generally similar variation to the

373   SSRI$_{grid}$, and the SSRIH$_{grid}$ usually more representative of climate change than SSRI$_{grid}$ at individual

374   stations.

375   Figure S5 (see in the SM) illustrates the long-term variations of global (Figure S5 (a) in the SM) and

376   continental land SSR (Figure S5 (b) in the SM) from the SSRI$_{grid}$ and SSRIH$_{grid}$ (except for Antarctica)

377   during 1955-2018. The most prominent change revolves around the adjustment around 1992: the SSR

378   anomalies were systematically adjusted upward from 1987 to 1992, while the SSR anomalies were

379   systematically adjusted downward from 1993 onwards. Thus, there is a significant decreasing trend for

380   both global land SSRI$_{grid}$ (-1.995 $\pm$ 0.251 W/m^2 per decade) and global land SSRIH$_{grid}$ (-1.776 $\pm$ 0.230

381   W/m^2 per decade) (except for Antarctica) from 1955 to 1991. While the increasing trend of the global

382   land SSRIH$_{grid}$ from 1991 to 2018 is 0.851 $\pm$ 0.410 W/m^2 per decade, slightly smaller than the increasing

383   trend of the SSRI$_{grid}$ (0.999 $\pm$ 0.504 W/m^2 per decade). It is worth noting that 1992 happened to be the

384   second year of the eruption of Mount Pinatubo, and the homogenized SSR data integrated in this paper

385   may be affected by this event. But overall, the homogenization also has limited effects on the global SSR

386   variations from Figure S5 (see in the SM), which is consistent with the influence of data homogenization

387   on a wide range of surface air temperatures (Brohan et al., 2006; Xu et al., 2013).

388   At the regional scale, the differences between the SSRIH$_{grid}$ and SSRI$_{grid}$ are more pronounced in Asia

389   and Europe (see Figure S5(b)in the SM). Asia's homogenized SSR show that the regional average SSR

390   has been declining significantly over the period 1958-90; this dimming trend mostly diminished over the

391   period 1991-2005 and was replaced by a brightening trend in the recent decade. The SSRIH$_{grid}$ in Asia is

392   higher than the SSRI$_{grid}$ from 1985 to 1990 and lower than the SSRI$_{grid}$ from 2012 to 2015. The SSRIH$_{grid}$

393   shows a more moderate short-term increase in Europe from 1960 to 1980. Note also that the Australian

394   raw data prior to 1988 were artificially detrended because at the time the Australia Weather Service was

395   afraid that the instruments would drift. Therefore, they detrended them and unfortunately did not store

396   the raw data, and the SSR evolution in Australia is artificial with no trend (Wild et al., 2005). In addition,

397   the SSRI$_{station}$ and SSRIH$_{station}$ comparisons for all 66 stations are shown in Figure S1 (see in the SM).

5 AI reconstruction and comparison

5.1 Training of the AI model

We produce two (20CRv3 /CMIP6) separate training and validation sets: we select the 1th member data of the reanalysis data and the model data, respectively, as the validation set, and the remaining 79 (124) ensemble members as the training sets, where each ensemble member included 732 (720) months of SSR data. Each validation set included 732 (720) samples, while the training sets contained 57828 (89280) ensemble members. All the above data, including the *in situ* observations, are then resampled to monthly anomalies of $5° \times 2.5°$.

We reconstruct the SSR of 20CRv3 /CMIP6 with missing values based on 20CRv3 /CMIP6 datasets using the method in section 3.2 and obtain two reconstructions, SSR_{20CR} and SSR_{CMIP6}, respectively. The SSR of 20CRv3/CMIP6 with missing values uses the $SSRIH_{grid}$ mask between 1955 and 2015 /2014. We compare the global land (except for Antarctica) /regional annual anomalies variation of SSR_{20CR} /SSR_{CMIP6}. The results show that SSR_{20CR} is significantly more consistent with the validation set than SSR_{CMIP6}.

Figure 6(a) shows that the RMSE/CC of the SSR_{20CR} (0.247 W/m^2 /0.970 W/m^2) are smaller /larger than those of SSR_{CMIP6} (0.518 W/m^2 /0.937 W/m^2) with the original 20CR /CMIP6 dataset. The 20CR-AI model has a better reconstruction ability for SSR at the global land (except for Antarctica) scale. The RMSEs of the SSR_{20CR} (SSR_{CMIP6}) are 1.460 (2.413) W/m^2, 1.109 (1.829) W/m^2, 2.219 (2.596) W/m^2 and 1.286 (2.235) W/m^2 in North America, Europe, Asia, and Northern Hemisphere, whereas these values are 1.116 (1.766) W/m^2, 0.622 (1.602) W/m^2, 1.877 (1.839) W/m^2 and 0.772 (1.679) W/m^2 in South America, Africa, Australia, and Southern Hemisphere concerning the original 20CR /CMIP6 dataset, respectively. In other words, the RMSEs of the SSR_{20CR} are smaller than those of $SSR_{CMIP6}$for the original 20CR /CMIP6 dataset except for Australia. In addition, the CCs of the SSR_{20CR} (SSR_{CMIP6}) are 0.958 (0.830) W/m^2, 0.958 (0.987) W/m^2, 0.886 (0.669) W/m^2, 0.930 (0.965) W/m^2, 0.938 (0.930) W/m^2, 0.943 (0.916) W/m^2, 0.936 (0.875) W/m^2 and 0.903 (0.822) W/m^2 in North America, Europe, Asia, Northern Hemisphere, South America, Africa, Australia, and Southern Hemisphere with respect to the original 20CR /CMIP6 dataset, respectively. That is, the CCs of the SSR_{20CR} are larger than those of $SSR_{CMIP6}$to the original 20CR /CMIP6 dataset except for Europe.

426   Based on the above comparison, the higher uncertainty for CMIP6 model output possibly biases the

427 CMIP6-AI method. Thus, the accuracy of the SSR_{20CR} is higher than that of the SSR_{CMIP6} at both global

428 land (except for Antarctica) and regional scales. Therefore, we choose the reconstruction results of the

429 20CR-AI model as the final AI reconstruction dataset, and subsequent analysis in the following sections

430 is only based on this dataset.

431 **5.2 Comparison of the spatial and temporal variation characteristics**

432 We investigate the long-term trends and spatial and temporal variation of the $SSRIH_{20CR}$, compare the

433 differences between the $SSRIH_{20CR}$ and $SSRIH_{grid}$, and suggest: the area and magnitude of the high and

434 low centres of the $SSRIH_{20CR}$ are the same as those of the $SSRIH_{grid}$; the results of the global land (except

435 for Antarctica) reconstruction are consistent with "dimming and brightening"; the global dimming is

436 primarily dominated by decreasing trends in Asia, Europe Africa and North America, whereas Europe

437 and North America are contributors to the increasing trends.

438   Figure 7 shows the spatial distribution of the $SSRIH_{grid}$ and $SSRIH_{20CR}$ for the three months (July 1960,

439 July 1980, and July 2000). Figure S6 (see in the SM) displays the spatial distribution of annual $SSRIH_{grid}$

440 and $SSRIH_{20CR}$ from 1955 to 2018. Figure 7 also shows the area and the magnitude of the high and low

441 centres in the $SSRIH_{20CR}$ are the same as in the $SSRIH_{grid}$. The $SSRIH_{20CR}$ is mainly positive anomalies

442 in Africa and the Eurasian continent in July 1960, especially in India and the Middle East. Afterwards,

443 India showed a continuous and steady decline in SSR. This confirms the well-known phenomenon of

444 global dimming over India (Wild et al., 2009; Soni et al., 2016; Soni et al., 2012; Padma Kumari et al.,

445 2007; Kambezidis et al., 2012). In Australia, the $SSRIH_{20CR}$ is dominated by negative anomalies in July

446 1980 and positive anomalies in July 1960 and July 2000. In Greenland, the $SSRIH_{20CR}$ shows a large

447 positive anomaly during three months. In northern Russia, there is a high value in July 2000. The

448 reconstruction can better reflect the anomaly distribution of observation information, and the grid boxes

449 with the missing values are infilled and reconstructed, which has high reliability.

450   Figure 8 illustrates global land (except for Antarctica) annual anomalies variation and long-term trend

451 of the $SSRIH_{20CR}$ for the period of 1955-2018, 1955-1991 and 1991-2018. Table S3 in the SM

452 demonstrates the trends of global SSR change evaluation for various data sources on different scales.

453 Also, we compare the differences between the $SSRIH_{20CR}$ and $SSRIH_{grid}$. The minimum value of the

454 $SSRIH_{20CR}$ occurred in 1991 (-2.411 W/m^2). The decreasing trend of the $SSRIH_{20CR}$ from 1955 to 1991

455   (-1.276 $\pm$ 0.205 W/m^2 per decade) is slightly lower than that of the SSRIH$_{grid}$ (-1.776 $\pm$ 0.230 W/m^2 per

456   decade). After that, the SSRIH$_{20CR}$ turns to an increasing trend of 0.697 $\pm$ 0.359 W/m^2 per decade from

457   1991 to 2018. This suggests that the difference between SSRIH$_{20CR}$ and SSRIH$_{grid}$ may be caused by the

458   results observed in limited data coverage (such as in Africa and North America) (Figure 9). After

459   homogenization and reconstruction, the trend (-1.276 W/m^2 per decade) from 1955 to 1991 corresponds

460   to an overall reduction of -4.6 W/m^2 over the dimming period, while that (0.697 W/m^{2}per decade) from

461   1991 to 2018 correspond to an overall increase of 2 W/m^2 over the brightening period. This is in amazing

462   agreement with the -4 W/m^2 for the dimming period and the 2 W/m^2 for the brightening period based on

463   an overall surface energy budget assessment ((Wild, 2012) see their Figure 1). Also, similar conclusions

464   (incomplete coverage of observational data lead to an underestimation of global warming trends) have

465   been confirmed in global warming research (Gulev et al., 2021; Li et al., 2021).

466   Figure 9 demonstrates the long-term annual anomaly variations of the SSRIH$_{20CR}$ in different regions

467   and its results compared to the SSRIH$_{grid}$. Table S4 in the SM shows the evaluation in continental and

468   hemispheric SSRIH$_{20CR}$ change trends on different scales. The SSRIH$_{20CR}$ shows a similar annual

469   anomaly variation to the global land (except for Antarctica) average trend in North America and Asia,

470   reaches a minimum in the late 1970s or early 1990s, and follows a moderate reversal. In Europe, the

471   SSRIH$_{20CR}$ shows a decrease (-2.180 $\pm$ 1.866 W/m^2 per decade) between 1963 and 1978 before turning

472   to brightening (1.081 $\pm$ 0.312 W/m^2 per decade). In South America and Australia (Southern Hemisphere),

473   the SSRIH$_{20CR}$ shows no significant variation. In Africa, the SSRIH$_{20CR}$ has a dimming trend (-1.506 $\pm$

474   0.496 W/m^2 per decade) from the 1950s to the 1990s, after which it remains levelled off (0.340 $\pm$ 0.998

475   W/m^2 per decade). The SSRIH$_{20CR}$ shows a decreasing trend (-1.457 $\pm$ 0.246 W/m^2 per decade) until the

476   1990s in the Northern Hemisphere and a brightening (0.887 $\pm$ 0.415 W/m^2 per decade) afterwards. The

477   annual average anomaly variations in regions and globally show that Asia, Africa, Europe and North

478   America are the four contributors to the global dimming, while Europe and North America are two major

479   contributors to the "brightening". This is in general agreement with the results obtained by previous

480   machine learning (Yuan et al., 2021). In addition, the discrepancy between the SSRIH$_{20CR}$ and SSRIH$_{grid}$

481   is more significant in low-coverage areas (right) than in high-coverage regions (left). It is particularly

482   pronounced before 1980 and in South America. This suggests that the limited surface observations are

483   not representative of the continental variation in SSR.

484   The sources of error in the observational dataset can be divided into three types: (1) station error, the

485 uncertainties of individual station anomalies; Including measurement errors (which are not the focus of

486 the considerations in this manuscript) and errors due to homogenization. The errors due to

487 homogenization adjustment are always approximately normally distributed ((Jones et al., 2008), see

488 their Figure 5; also see Figure S9 in the SM) and therefore have limited impacts on the global average

489 SSR change (Figure S5 a, b). (2) sampling error, the uncertainties in a grid box mean caused by

490 estimating the mean from a small number of point values (Jones et al., 1997) ; and (3) bias error. It

491 generally refers to systematic errors such as urbanization together, which has not been discussed here.

492 However, even the sum of the above errors is much smaller than the errors due to limited data coverage

493 ((Li et al., 2010), see their Figure 5). So, the focus of this study is to eliminate this kind of error through

494 the CNN reconstruction.

495 **6 Data availability**

496 Both the $SSRIH_{grid}$ (the homogenized monthly gridded SSR data over 1923-2020) and the $SSRIH_{20CR}$

497 (the monthly 20CR-AI model reconstructed SSR data for 1955-2018) are currently publicly available on

498 the figshare website under DOI at https://doi.org/10.6084/m9.figshare.21625079.v1 (Jiao and Li, 2023).

499 These datasets are also available at http://www.gwpu.net for free.

500 **7 Conclusion**

501 In this study, we integrate global station observations based on the raw observational SSRs from GEBA

502 and WRDC, combined with existing homogenized SSR datasets from other scholars. Also, we

503 homogenize the globally distributed station data using the RHtestV4 software package. An improved

504 CNN deep learning algorithm is subsequently used to reconstruct the SSR anomalies. Thus, a

505 reconstructed SSR anomaly dataset, $SSRIH_{20CR}$, is obtained based on training sets (20CRv3), for the

506 years 1955-2018, with a resolution of $5°×2.5°$. The main results are as follows:

507 1) The first integrated and homogenized global SSR monthly dataset is developed, which contains 944

508 stations in total and covers the longest periods (from the 1920s to recent years). A $5°×5°$ grid boxes

509 version of the monthly SSR anomalies dataset is derived.

510 2) This paper develops $5°×2.5°$ full-coverage monthly land (except for Antarctica) SSR anomalies

511 reconstructed datasets based on the above observations, using the 20CRv3 to train the AI model.

512 Comparative validations /evaluations show that the $SSRIH_{20CR}$ provides a reliable benchmark for global

513 SSR variations.

514   3) On average, the global annual SSR variations based on the $SSRIH_{grid}$ are not significantly different,

515 except that the increasing (brightening) trend after 1991 is a little smaller for the latter. The short-term

516 brightening SSR in Europe from the 1970s- to the 1980s disappear at the regional scale. At the same time,

517 the brightening SSR after the 1990s in Asia slowed or postponed.

518 **Author contributions**

519 Boyang Jiao: Software, Data curation, Writing- Original draft preparation, Visualization, Investigation.

520 Yucheng Su: Software, Data curation.

521 Qingxiang Li: Methodology, Supervision, Conceptualization, Validation, Writing - Review and Editing.

522 Veronica Manara: Providing the homogenized Italian dataset, Writing - Review and Editing.

523 Martin Wild: Writing - Review and Editing.

524 **Competing interests**

525 At least one of the (co-) authors is a member of the editorial board of Earth System Science Data.

526 **Disclaimer**

527 Publisher's note: Copernicus Publications remains neutral about jurisdictional claims in published maps

528 and institutional affiliations.

529 **Financial support**

530 This study is supported by the Natural Science Foundation of China (Grant: 41975105) and the National

531 Key R&D Program of China (Grant: 2018YFC1507705; 2017YFC1502301). The Global Energy

532 Balance Archive (GEBA) is co-funded by the Federal Office of Meteorology and Climatology

533 MeteoSwiss within the framework of GCOS Switzerland. Global dimming and brightening research at

534 ETH Zurich are supported by the Swiss National Science Foundation (Grant No. 200020 188601).

535 Veronica Manara was supported by the "Ministero dell'Università e della Ricerca" of Italy [grant FSE –

536 REACT EU, DM 10/08/2021 n. 1062].

537   **Reference**

538   Aguiar, L. M., Pereira, B., David, M., Díaz, F., and Lauret, P.: Use of satellite data to improve solar

539   radiation forecasting with Bayesian Artificial Neural Networks, Solar Energy, 122, 1309-1324,

540   doi:10.1016/j.solener.2015.10.041, 2015.

541   Alexandersson, H.: A homogeneity test applied to precipitation data, Journal of Climatology, 6, 661-675,

542   doi:10.1002/joc.3370060607, 1986.

543   Bookstein, F. L.: Principal warps: Thin-plate splines and the decomposition of deformations, IEEE

544   Transactions on pattern analysis and machine intelligence, 11, 567-585, doi:10.1109/34.24792, 1989.

545   Brohan, P., Kennedy, J. J., Harris, I., Tett, S. F. B., and Jones, P. D.: Uncertainty estimates in regional and

546   global observed temperature changes: A new data set from 1850, Journal of Geophysical Research:

547   Atmospheres, 111, doi:10.1029/2005JD006548, 2006.

548   Cao, Y., Jiao, B., Lan, X., Tan, J., Yang, Y., Sun, W., Li, Z., Luo, J., and Li, Q.: Reconstruction og China

549   global Merged Surface Temperature (CMST) based on an artifical intelligence approach

550   (submitted), Enviormental Scinence & Technology, 2022.

551   Collins, F. C.: A comparison of spatial interpolation techniques in temperature estimation, The 3rd

552   International Conference/Workshop on Integrating GIS and Environmental Modeling, Santa

553   Barbara, Santa Fe, NM; Santa Barbara, CA, 21-26 January1996 of Conference.

554   Craddock, J. M.: Methods of comparing annual rainfall records for climatic purposes, Weather, 34, 332-

555   346, doi:10.1002/j.1477-8696.1979.tb03465.x, 1979.

556   Driemel, A., Augustine, J., Behrens, K., Colle, S., Cox, C., Cuevas-Agulló, E., Denn, F. M., Duprat, T.,

557   Fukuda, M., and Grobe, H.: Baseline Surface Radiation Network (BSRN): structure and data

558   description (1992–2017), Earth System Science Data, 10, 1491-1501, doi:10.5194/essd-10-1491-

559   2018, 2018.

560   Erxleben, J., Elder, K., and Davis, R.: Comparison of spatial interpolation methods for estimating snow

561   distribution in the Colorado Rocky Mountains, Hydrological Processes, 16, 3627-3649,

562   doi:10.1002/hyp.1239, 2002.

563   Evan, A. T., Heidinger, A. K., and Vimont, D. J.: Arguments against a physical long-term trend in global

564   ISCCP cloud amounts, Geophysical Research Letters, 34, 10.1029/2006gl028083, 2007.

565   Eyring, V., Bony, S., Meehl, G. A., Senior, C. A., Stevens, B., Stouffer, R. J., and Taylor, K. E.: Overview

566   of the Coupled Model Intercomparison Project Phase 6 (CMIP6) experimental design and

567   organization, Geoscientific Model Development, 9, 1937-1958, doi:10.5194/gmd-9-1937-2016,

568   2016.

569 Feng, F. and Wang, K.: Merging high-resolution satellite surface radiation data with meteorological

570   sunshine duration observations over China from 1983 to 2017, Remote Sensing, 13, 602,

571   doi:10.3390/rs13040602, 2021.

572 Fisher, N. I., Lewis, T., and Embleton, B. J.: Statistical analysis of spherical data, Cambridge university

573   press, doi:10.1017/CBO9780511623059, 1993.

574 Fukami, K., Fukagata, K., and Taira, K.: Machine-learning-based spatio-temporal super resolution

575   reconstruction of turbulent flows, Journal of Fluid Mechanics, 909, doi:10.1017/jfm.2020.948, 2021.

576 Gates, W. L., Boyle, J. S., Covey, C., Dease, C. G., Doutriaux, C. M., Drach, R. S., Fiorino, M., Gleckler,

577   P. J., Hnilo, J. J., Marlais, S. M., Phillips, T. J., Potter, G. L., Santer, B. D., Sperber, K. R., Taylor,

578   K. E., and Williams, D. N.: An Overview of the Results of the Atmospheric Model Intercomparison

579   Project (AMIP I), Bulletin of the American Meteorological Society, 80, 29-55, 10.1175/1520-

580   0477(1999)080<0029:Aootro>2.0.Co;2, 1999.

581 Gulev, S. K., Thorne, P. W., J. Ahn, F. J. D., Domingues, C. M., Gerland, S., Gong, D., Kaufman, D. S.,

582   Nnamchi, H. C., Quaas, J., Rivera, J. A., Sathyendranath, S., Smith, S. L., Trewin, B., Shuckmann,

583   K. v., and Vose, R. S.: In: Climate Change 2021: The Physical Science Basis., Climate Change 2021:

584   The Physical Science Basis. Contribution of Working Group I to the Sixth Assessment Report of the

585   Intergovernmental Panel on Climate Change, in, edited by: [Masson-Delmotte, V., Zhai, P., Pirani,

586   A., Connors, S. L., Péan, C., Berger, S., Caud, N., Chen, Y., Goldfarb, L., Gomis, M. I., Huang, M.,

587   Leitzell, K., Lonnoy, E., Matthews, J. B. R., Maycock, T. K., Waterfield, T., Yelekçi, O., Yu, R., and

588   (eds.)], B. Z., Cambridge University Press. 2021., 287–422. Cambridge University Press, 2021.

589 He, J., Hong, L., Shao, C., and Tang, W.: Global evaluation of simulated surface shortwave radiation in

590   CMIP6 models, Atmospheric Research, 292, 10.1016/j.atmosres.2023.106896, 2023.

591 He, Y., Wang, K., and Feng, F.: Improvement of ERA5 over ERA-Interim in simulating surface incident

592   solar radiation throughout China, Journal of Climate, 34, 3853-3867, 2021.

593 Hersbach, H., Bell, B., Berrisford, P., Hirahara, S., Horányi, A., Muñoz-Sabater, J., Nicolas, J., Peubey,

594   C., Radu, R., Schepers, D., Simmons, A., Soci, C., Abdalla, S., Abellan, X., Balsamo, G., Bechtold,

595   P., Biavati, G., Bidlot, J. R., Bonavita, M., Chiara, G. D., Dahlgren, P., Dee, D., Diamantakis, M.,

Dragani, R., Flemming, J., Forbes, R. G., Fuentes, M., Geer, A. J., Haimberger, L., Healy, S. B., Hogan, R. J., Holm, E. V., Janisková, M., Keeley, S. P. E., Laloyaux, P., Lopez, P., Lupu, C., Radnoti, G., Rosnay, P. d., Rozum, I., Vamborg, F., Villaume, S., and Thepaut, J.-N.: The ERA5 global reanalysis, Quarterly Journal of the Royal Meteorological Society, 146, 1999 - 2049, doi:10.1002/qj.3803, 2020.

Hoskins, B. J. and Valdes, P. J.: On the existence of storm-tracks, Journal of Atmospheric Sciences, 47, 1854-1864, doi:10.1175/1520-0469(1990)047<1854:OTEOST>2.0.CO;2, 1990.

Huang, B., Yin, X., Menne, M. J., Vose, R., and Zhang, H.-M.: Improvements to the Land Surface Air Temperature Reconstruction in NOAAGlobalTemp: An Artificial Neural Network Approach, Artificial Intelligence for the Earth Systems, 1-35, doi:10.1175/AIES-D-22-0032.1, 2022.

Huang, J., Rikus, L. J., Qin, Y., and Katzfey, J.: Assessing model performance of daily solar irradiance forecasts over Australia, Solar Energy, 176, 615-626, 10.1016/j.solener.2018.10.080, 2018.

Jiao, B. and Li, Q.: Global Integrated and Homogenized Solar surface Radiation Datasets, doi:10.6084/m9.figshare.21625079.v1, 2023.

Jiao, B., Li, Q., Sun, W., and Martin, W.: Uncertainties in the global and continental surface solar radiation variations: inter-comparison of in-situ observations, reanalyses, and model simulations, Climate Dynamics, 1-18, doi:10.1007/s00382-022-06222-3, 2022.

Jones, P., Osborn, T., Briffa, K., Folland, C., Horton, E., Alexander, L., Parker, D., and Rayner, N.: Adjusting for sampling density in grid box land and ocean surface temperature time series, Journal of Geophysical Research: Atmospheres, 106, 3371-3380, doi:10.1029/2000JD900564, 2001.

Jones, P. D., Lister, D. H., and Li, Q.: Urbanization effects in large-scale temperature records, with an emphasis on China, Journal of Geophysical Research, 113, 10.1029/2008jd009916, 2008.

Jones, P. D., Osborn, T. J., and Briffa, K. R.: Estimating Sampling Errors in Large-Scale Temperature Averages, Journal of Climate, 10, 2548-2568, 1997.

Ju, X., Tu, Q., and Li, Q.: Homogeneity test and reduction of monthly total solar radiation over China, J Nanjing Inst Meteorol, 29, 336-341, 2006.

Kadow, C., Hall, D. M., and Ulbrich, U.: Artificial intelligence reconstructs missing climate information, Nature Geoscience, 13, 408-413, doi:10.1038/s41561-020-0582-5, 2020.

Kambezidis, H. D., Kaskaoutis, D. G., Kharol, S. K., Moorthy, K. K., Satheesh, S. K., Kalapureddy, M. C. R., Badarinath, K. V. S., Sharma, A. R., and Wild, M.: Multi-decadal variation of the net

downward shortwave radiation over south Asia: The solar dimming effect, Atmospheric Environment, 50, 360-372, 2012.

Krige, D. G.: A statistical approach to some basic mine valuation problems on the Witwatersrand, Journal of the Southern African Institute of Mining and Metallurgy, 52, 119-139, doi:10.10520/AJA0038223X_4792, 1951.

Leirvik, T. and Yuan, M.: A machine learning technique for spatial interpolation of solar radiation observations, Earth and Space Science, 8, e2020EA001527, doi:10.1029/2020EA001527, 2021.

Li, Q., Dong, W., Li, W., Gao, X., Jones, P., Kennedy, J., and Parker, D.: Assessment of the uncertainties in temperature change in China during the last century, Chinese Science Bulletin, 55, 1974-1982, 10.1007/s11434-010-3209-1, 2010.

Li, Q., Sun, W., Yun, X., Huang, B., Dong, W., Wang, X. L., Zhai, P., and Jones, P.: An updated evaluation of the global mean land surface air temperature and surface temperature trends based on CLSAT and CMST, Climate Dynamics, 56, 635-650, doi: 10.1007/s00382-020-05502-0, 2021.

Liang, H., Jiang, B., Liang, S., Peng, J., Li, S., Han, J., Yin, X., Cheng, J., Jia, K., and Liu, Q.: A global long-term ocean surface daily/0.05° net radiation product from 1983–2020, Scientific Data, 9, 1-17, doi:10.1038/s41597-022-01419-x, 2022.

Ma, Q., Wang, K., He, Y., Su, L., Wu, Q., Liu, H., and Zhang, Y.: Homogenized century-long surface incident solar radiation over Japan, Earth System Science Data, 14, 463-477, doi:10.5194/essd-14-463-2022, 2022.

Manara, V., Bassi, M., Brunetti, M., Cagnazzi, B., and Maugeri, M.: 1990–2016 surface solar radiation variability and trend over the Piedmont region (northwest Italy), Theoretical and Applied Climatology, 136, 849-862, doi:10.1007/s00704-018-2521-6, 2019.

Manara, V., Brunetti, M., Celozzi, A., Maugeri, M., Sanchez-Lorenzo, A., and Wild, M.: Detection of dimming/brightening in Italy from homogenized all-sky and clear-sky surface solar radiation records and underlying causes (1959–2013), Atmospheric Chemistry and Physics, 16, 11145-11161, doi:10.5194/acp-16-11145-2016, 2016.

Manara, V., Stocco, E., Brunetti, M., Diolaiuti, G. A., Fugazza, D., Pfeifroth, U., Senese, A., Trentmann, J., and Maugeri, M.: Comparison of Surface Solar Irradiance from Ground Observations and Satellite Data (1990–2016) over a Complex Orography Region (Piedmont—Northwest Italy), Remote Sensing, 12, 3882, 2020.

656   Manara., V., Michele., B., ., M. M., ., S.-L. A., and Martin, W.: Homogenization of a surface solar

657   radiation dataset over Italy, AIP Conference Proceedings, 22 February 2017, doi:

658   org/10.1063/1.4975544, 2017.

659   Mlawer, E. J., Taubman, S. J., Brown, P. D., Iacono, M. J., and Clough, S. A.: Radiative transfer for

660   inhomogeneous atmospheres: RRTM, a validated correlated-k model for the longwave, Journal of

661   Geophysical Research: Atmospheres, 102, 16663-16682, https://doi.org/10.1029/97JD00237, 1997.

662   Olanow, C. W. and Koller, W. C.: An algorithm (decision tree) for the management of Parkinson's disease:

663   Treatment guidelines, Neurology, 50, S1-s88, 1998.

664   Padma Kumari, B., Londhe, A. L., Daniel, S., and Jadhav, D. B.: Observational evidence of solar

665   dimming: Offsetting surface warming over India, Geophysical Research Letters, 34,

666   https://doi.org/10.1029/2007GL031133, 2007.

667   Peixoto, J. P., Oort, A. H., and Lorenz, E. N.: Physics of climate, Springer1992.

668   Peterson, T. C., Karl, T. R., Jamason, P. F., Knight, R., and Easterling, D. R.: First difference method:

669   Maximizing station density for the calculation of long-term global temperature change, Journal of

670   Geophysical Research: Atmospheres, 103, 25967-25974, doi:10.1029/98JD01168, 1998.

671   Pfeifroth, U., Sanchez-Lorenzo, A., Manara, V., Trentmann, J., and Hollmann, R.: Trends and Variability

672   of Surface Solar Radiation in Europe Based On Surface- and Satellite-Based Data Records, Journal

673   of Geophysical Research: Atmospheres, 123, 1735-1754, doi: 10.1002/2017JD027418, 2018.

674   Ronneberger, O., Fischer, P., and Brox, T.: U-net: Convolutional networks for biomedical image

675   segmentation, International Conference on Medical image computing and computer-assisted

676   intervention, 234-241, doi:10.48550/arXiv.1505.04597,

677   Sanchez-Lorenzo, A., Calbó, J., and Wild, M.: Global and diffuse solar radiation in Spain: Building a

678   homogeneous dataset and assessing their trends, Global and Planetary Change, 100, 343-352,

679   doi:10.1016/j.gloplacha.2012.11.010, 2013a.

680   Sanchez-Lorenzo, A., Wild, M., and Trentmann, J.: Validation and stability assessment of the monthly

681   mean CM SAF surface solar radiation dataset over Europe against a homogenized surface dataset

682   (1983–2005), Remote sensing of environment, 134, 355-366, doi:10.1016/j.rse.2013.03.012, 2013b.

683   Sanchez-Lorenzo, A., Wild, M., Brunetti, M., Guijarro, J. A., Hakuba, M. Z., Calbó, J., Mystakidis, S.,

684   and Bartok, B.: Reassessment and update of long-term trends in downward surface shortwave

685   radiation over Europe (1939–2012), Journal of Geophysical Research: Atmospheres, 120, 9555-

686   9569, doi:10.1002/2015JD023321, 2015.

687   Scudiero, E., Corwin, D. L., Morari, F., Anderson, R. G., and Skaggs, T. H.: Spatial interpolation quality

688   assessment for soil sensor transect datasets, Computers and Electronics in Agriculture, 123, 74-79,

689   doi:10.1016/j.compag.2016.02.016, 2016.

690   Shao, C., Yang, K., Tang, W., He, Y., Jiang, Y., Lu, H., Fu, H., and Zheng, J.: Convolutional neural

691   network-based homogenization for constructing a long-term global surface solar radiation dataset,

692   Renewable and Sustainable Energy Reviews, 169, 10.1016/j.rser.2022.112952, 2022.

693   Shepard, D.: A two-dimensional interpolation function for irregularly-spaced data, Proceedings of the

694   1968 23rd ACM national conference, 517-524,   doi:10.1145/800186.810616,

695   Slivinski, L. C., Compo, G. P., Whitaker, J. S., Sardeshmukh, P. D., Giese, B. S., McColl, C., Allan, R.,

696   Yin, X., Vose, R., and Titchner, H.: Towards a more reliable historical reanalysis: Improvements for

697   version 3 of the Twentieth Century Reanalysis system, Quarterly Journal of the Royal

698   Meteorological Society, 145, 2876-2908, doi:10.1002/qj.3598, 2019.

699   Soni, V. K., Pandithurai, G., and Pai, D. S.: Evaluation of long-term changes of solar radiation in India,

700   International Journal of Climatology, 32, 540-551, https://doi.org/10.1002/joc.2294, 2012.

701   Soni, V. K., Pandithurai, G., and Pai, D. S.: Is there a transition of solar radiation from dimming to

702   brightening over India, Atmospheric Research, 169, 209-224, 2016.

703   Tang, W., Yang, K., Qin, J., Li, X., and Niu, X.: A 16-year dataset (2000–2015) of high-resolution (3 h,

704   10 km) global surface solar radiation, Earth System Science Data, 11, 1905-1915, doi:10.5194/essd-

705   11-1905-2019, 2019.

706   Tang, W., Qin, J., Yang, K., Liu, S., Lu, N., and Niu, X.: Retrieving high-resolution surface solar radiation

707   with cloud parameters derived by combining MODIS and MTSAT data, Atmospheric Chemistry

708   and Physics, 16, 2543-2557, doi:10.5194/acp-16-2543-2016, 2016.

709   Trenberth, K. E. and Fasullo, J. T.: Regional energy and water cycles: Transports from ocean to land,

710   Journal of Climate, 26, 7837-7851, doi:10.1175/JCLI-D-13-00008.1, 2013.

711   Tsvetkov, A., Wilcox, S., Renne, D., and Pulscak, M.: International solar resource data at the World

712   Radiation Data Center, American Solar Energy Society, Boulder, CO (United States), 1995.

713   Urraca, R., Huld, T., Martinez-de-Pison, F. J., and Sanz-Garcia, A.: Sources of uncertainty in annual

714   global horizontal irradiance data, Solar Energy, 170, 873-884, 10.1016/j.solener.2018.06.005, 2018.

715   Vincent, L. A., Wang, X. L., Milewska, E. J., Wan, H., Yang, F., and Swail, V.: A second generation of

homogenized Canadian monthly surface air temperature for climate trend analysis, Journal of Geophysical Research: Atmospheres, 117, doi:10.1029/2012JD017859, 2012.

Wang, K.: Measurement biases explain discrepancies between the observed and simulated decadal variability of surface incident solar radiation, Scientific reports, 4, 1-7, doi:0.1038/srep06144 2014.

Wang, K., Ma, Q., Li, Z., and Wang, J.: Decadal variability of surface incident solar radiation over China: Observations, satellite retrievals, and reanalyses, Journal of Geophysical Research: Atmospheres, 120, 6500-6514, doi:10.1002/2015JD023420, 2015.

Wang, X. L.: Accounting for autocorrelation in detecting mean shifts in climate data series using the penalized maximal t or F test, Journal of applied meteorology and climatology, 47, 2423-2444, doi:10.1175/2008JAMC1741.1, 2008a.

Wang, X. L.: Penalized maximal F test for detecting undocumented mean shift without trend change, Journal of Atmospheric and Oceanic Technology, 25, 368-384, doi:10.1175/2007JTECHA982.1, 2008b.

Wang, X. L. and Feng, Y.: RHtestsV4 user manual, Climate Research Division, Atmospheric Science and Technology Directorate, Science and Technology Branch, Environment Canada, 28, 2013.

Wang, X. L., Wen, Q. H., and Wu, Y.: Penalized maximal t test for detecting undocumented mean change in climate data series, Journal of Applied Meteorology and Climatology, 46, 916-931, doi:10.1175/JAM2504.1, 2007.

Wang, X. L., Chen, H., Wu, Y., Feng, Y., and Pu, Q.: New techniques for the detection and adjustment of shifts in daily precipitation data series, Journal of Applied Meteorology and Climatology, 49, 2416-2436, doi:10.1175/2010JAMC2376.1, 2010.

Wang, Y. and Wild, M.: A new look at solar dimming and brightening in China, Geophysical Research Letters, 43, 11,777-711,785, doi:10.1002/2016GL071009, 2016.

Wild, M.: Enlightening global dimming and brightening, Bulletin of the American Meteorological Society, 93, 27-37, doi:10.1175/BAMS-D-11-00074.1, 2012.

Wild, M.: The global energy balance as represented in CMIP6 climate models, Clim Dyn, 55, 553-577, 10.1007/s00382-020-05282-7, 2020.

Wild, M., Trüssel, B., Ohmura, A., Long, C. N., König-Langlo, G., Dutton, E. G., and Tsvetkov, A.: Global dimming and brightening: An update beyond 2000, Journal of Geophysical Research: Atmospheres, 114, https://doi.org/10.1029/2008JD011382, 2009.

746 Wild, M., Ohmura, A., Schär, C., Müller, G., Folini, D., Schwarz, M., Hakuba, M. Z., and Sanchez-
747   Lorenzo, A.: The Global Energy Balance Archive (GEBA) version 2017: A database for worldwide
748   measured surface energy fluxes, Earth System Science Data, 9, 601-613, doi:10.5194/essd-9-601-
749   2017, 2017.

750 Wild, M., Gilgen, H., Roesch, A., Ohmura, A., Long, C. N., Dutton, E. G., Forgan, B., Kallis, A., Russak,
751   V., and Tsvetkov, A.: From dimming to brightening: Decadal changes in solar radiation at Earth's
752   surface, Science, 308, 847-850, doi:10.1126/science.1103215, 2005.

753 Xu, W., Li, Q., Wang, X. L., Yang, S., Cao, L., and Feng, Y.: Homogenization of Chinese daily surface
754   air temperatures and analysis of trends in the extreme temperature indices, Journal of Geophysical
755   Research: Atmospheres, 118, 9708-9720, doi:10.1002/jgrd.50791, 2013.

756 Xu, W., Li, Q., Jones, P., Wang, X. L., Trewin, B., Yang, S., Zhu, C., Zhai, P., Wang, J., and Vincent, L.:
757   A new integrated and homogenized global monthly land surface air temperature dataset for the
758   period since 1900, Climate Dynamics, 50, 2513-2536, doi:10.1007/s00382-017-3755-1, 2018.

759 Yang, L., Zhang, X., Liang, S., Yao, Y., Jia, K., and Jia, A.: Estimating surface downward shortwave
760   radiation over China based on the gradient boosting decision tree method, Remote Sensing, 10, 185,
761   doi:10.3390/rs10020185, 2018a.

762 Yang, S.: Chinese Monthly homogenized   surface solar radiation datasets (V 1.0), 2016.

763 Yang, S., Wang, X. L., and Wild, M.: Homogenization and trend analysis of the 1958–2016 in situ surface
764   solar radiation records in China, Journal of Climate, 31, 4529-4541, doi:10.1175/JCLI-D-17-0891.1,
765   2018b.

766 You, Q., Sanchez-Lorenzo, A., Wild, M., Folini, D., Fraedrich, K., Ren, G., and Kang, S.: Decadal
767   variation of surface solar radiation in the Tibetan Plateau from observations, reanalysis and model
768   simulations, Climate dynamics, 40, 2073-2086, doi:10.1007/s00382-012-1383-3, 2013.

769 Yuan, M., Leirvik, T., and Wild, M.: Global trends in downward surface solar radiation from spatial
770   interpolated ground observations during 1961–2019, Journal of Climate, 34, 9501-9521,
771   doi:10.1175/JCLI-D-21-0165.1, 2021.

772 Zhou, C., He, Y., and Wang, K.: On the suitability of current atmospheric reanalyses for regional warming
773   studies over China, Atmospheric Chemistry and Physics, 18, 8113-8136, 10.5194/acp-18-8113-
774   2018, 2018a.

775 Zhou, C., Wang, K., and Ma, Q.: Evaluation of Eight Current Reanalyses in Simulating Land Surface

776   Temperature from 1979 to 2003 in China, Journal of Climate, 30, 7379-7398,

777   https://doi.org/10.1175/JCLI-D-16-0903.1, 2017.

778   Zhou, W., Gong, L., Wu, Q., Xing, C., Wei, B., Chen, T., Zhou, Y., Yin, S., Jiang, B., Xie, H., Zhou, L.,

779   and Zheng, S.: Correction to: PHF8 upregulation contributes to autophagic degradation of E-

780   cadherin, epithelial-mesenchymal transition and metastasis in hepatocellular carcinoma, Journal of

781   Experimental & Clinical Cancer Research, 37, 10.1186/s13046-018-0944-7, 2018b.

782   Zhou, W., Gong, L., Wu, Q., Xing, C., Wei, B., Chen, T., Zhou, Y., Yin, S., Jiang, B., Xie, H., Zhou, L.,

783   and Zheng, S.: Correction to: PHF8 upregulation contributes to autophagic degradation of E-

784   cadherin, epithelial-mesenchymal transition and metastasis in hepatocellular carcinoma, J Exp Clin

785   Cancer Res, 38, 445, 10.1186/s13046-019-1452-0, 2019.

786

787   **Captions of tables and Figures**

788   Table 1: List of information on the various types of data used in this paper.
789
790   Figure 1: Flowchart of quality control (QC) (first step), homogenization (second step) and integration
791   (third step).
792
793   Figure 2: Spatial distribution of candidate stations ("*") and added stations ("+"). The different colour
794   bars represent the length of the station record in months (Units: Month).
795
796   Figure 3: Spatial distribution of stations after homogenization (Units: Month), different colours
797   represent the length of station records in months
798
799   Figure 4: Flowchart of AI reconstruction.
800
801   Figure 5: (a) Spatial distribution of $5°\times5°$grid boxes (SSRIH$_{grid}$) obtained interpolating the
802   homogenized global land (except for Antarctica) SSR series. The different colours represent the length
803   (the sum of all records) of the station record, Units: Year. (b) Grid box coverage for the homogenized
804   global land (except for Antarctica) SSR (SSRIH$_{grid}$) except for Antarctica.
805
806   Figure 6: Reconstruction capabilities of the AI model.
807
808   Figure 7: Spatial distribution of the SSRIH$_{grid}$ (a1-3) and SSRIH$_{20CR}$ (b1-3) in typical months. 1-3 is
809   July 1960, July 1980, and July 2000, respectively.
810
811   Figure 8: Global land (except for Antarctica) time series of the annual anomaly variations SSR (relative
812   to 1971-2000) before/after reconstruction.
813
814   Figure 9: Same as Figure 8, but for regional annual anomaly variations.
815
816

817 **Table 1: List of information on the various types of data used in this paper**

	Abbreviation	Resolution	Time	Reference
In situ-Raw	GEBA (Station)	Monthly	1922-2020	(Wild et al., 2017)
	WRDC (Station)	Monthly	1964-2017	(Tsvetkov et al., 1995)
In situ-Homo	China (Station)	Monthly	1950-2016	(Yang et al., 2018b)
	Japan (Station)	Monthly	1870-2015	(Ma et al., 2022)
	Europe (Station)	Monthly	1922-2012	(Sanchez-Lorenzo et al., 2015)
	Italy (Station)	Monthly	1959-2016	(Manara et al., 2016; Manara et al., 2019)
Reanalysis / Model	ERA5 (Grid)	Monthly/ 0.25°×0.25°	1950-2020	(Hersbach et al., 2020)
	20CRv3 (Grid)	Monthly/ 0.7°×0.7°	1940-2015	(Slivinski et al., 2019)
	CMIP6 (Grid)	Monthly/-	1940-2014	(Eyring et al., 2016)

818
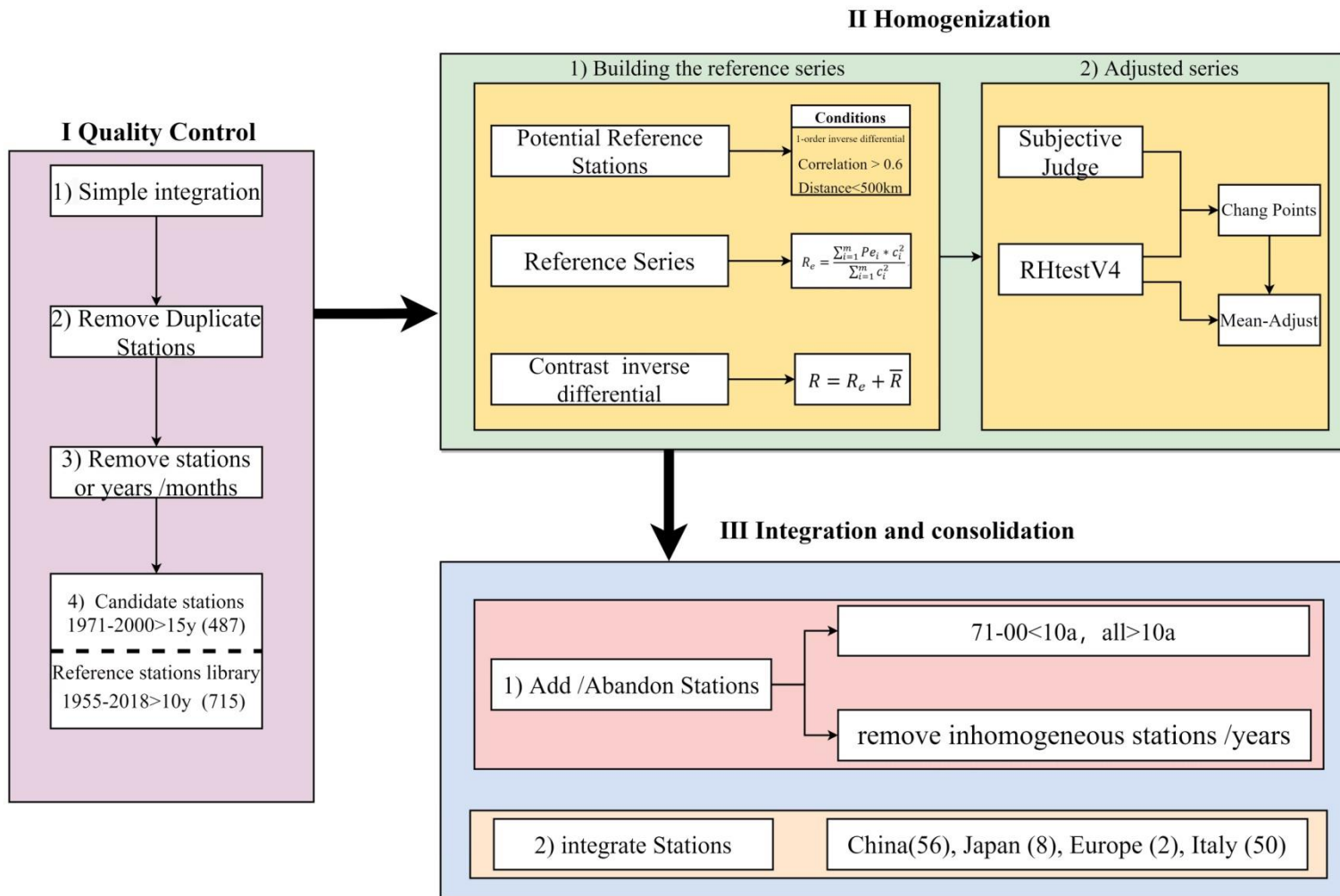
819

Figure 1: Flowchart of quality control (QC) (first step), homogenization (second step) and integration (third step).
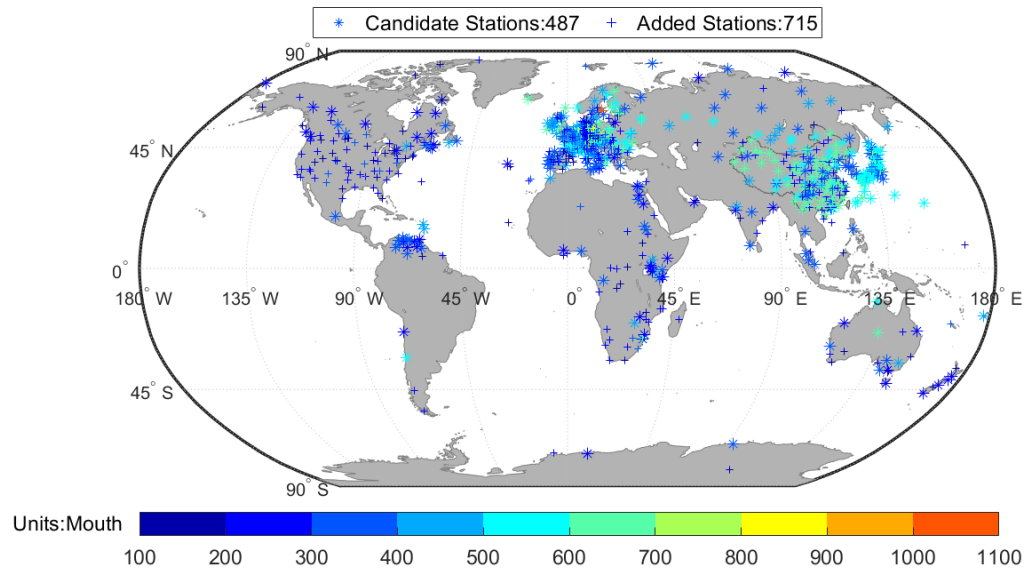
821

Figure 2: Spatial distribution of candidate stations ("*") and added stations ("+"). The different colour bars
represent the length of the station record in months (Units: Month).
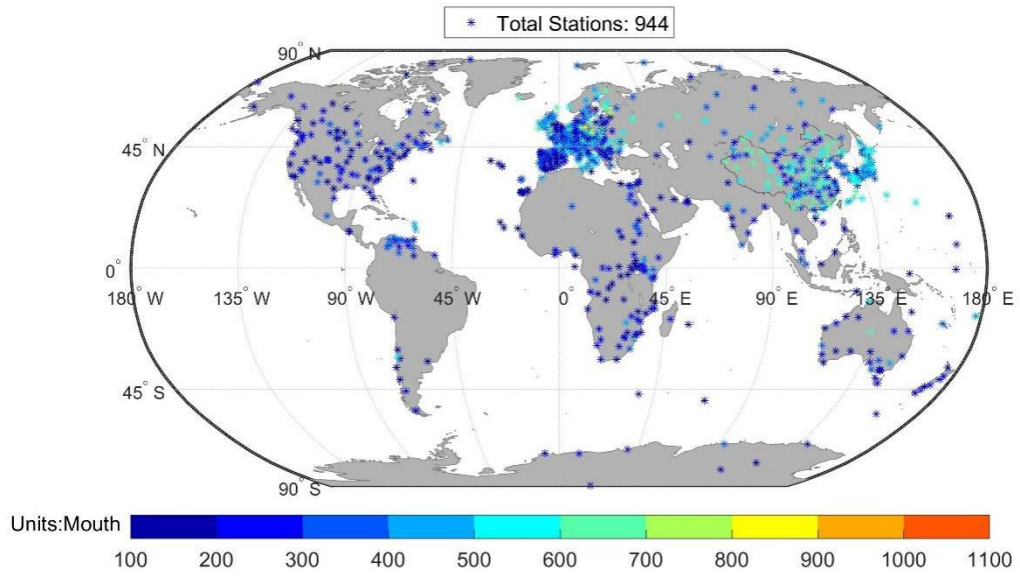
824
825 **Figure 3: Spatial distribution of stations after homogenization (Units: Month), different colours represent the**

826 **length of station records in months.**
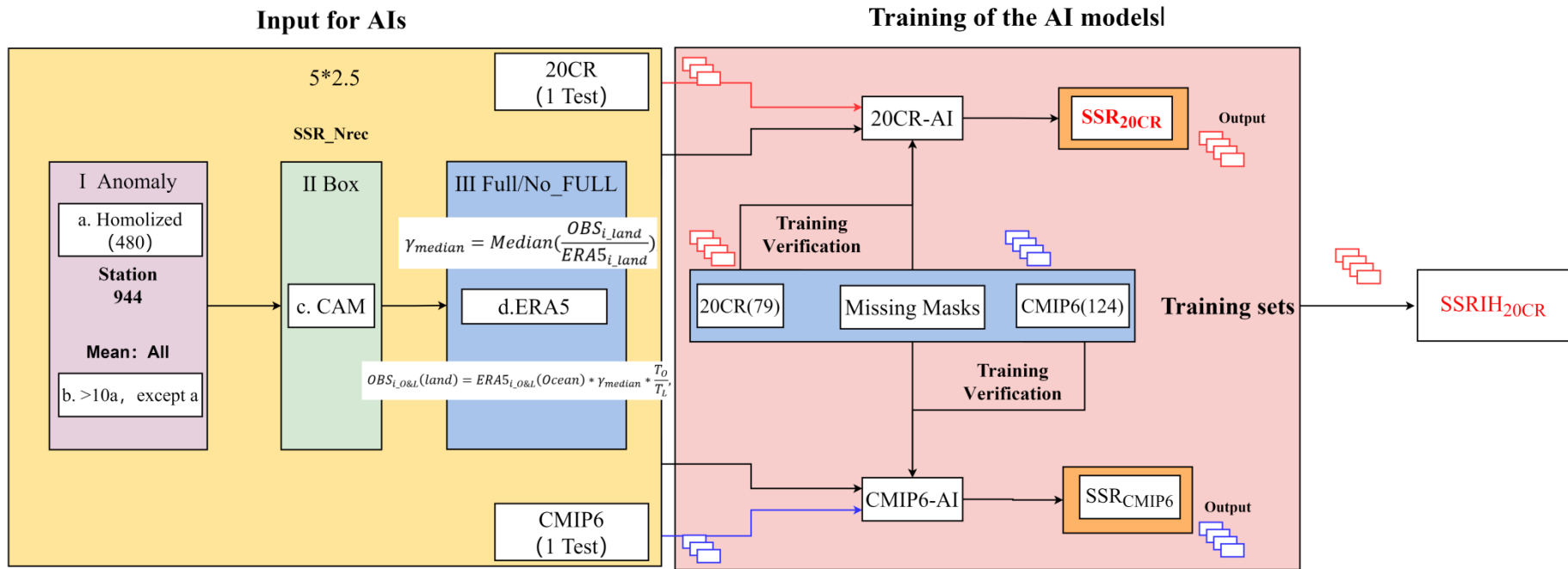
827

828 **Figure 4: Flowchart of AI reconstruction.**
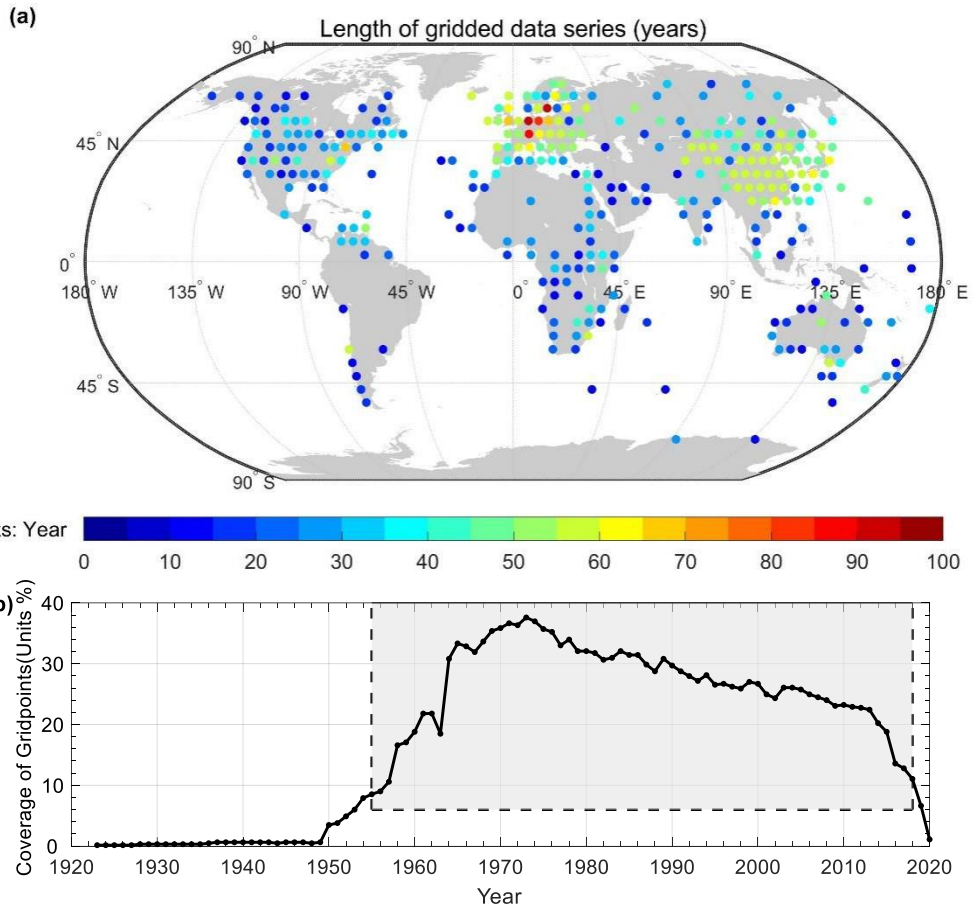
829

830

831 **Figure 5: (a) Spatial distribution of 5°×5°grid boxes (SSRIH_grid) obtained interpolating the homogenized**

832 **global land (except for Antarctica) SSR series. The different colours represent the length (the sum of all**

833 **records) of the station record, Units: Year. (b) Grid box coverage for the homogenized global land (except**

834 **for Antarctica) SSR (SSRIH_grid) except for Antarctica.**
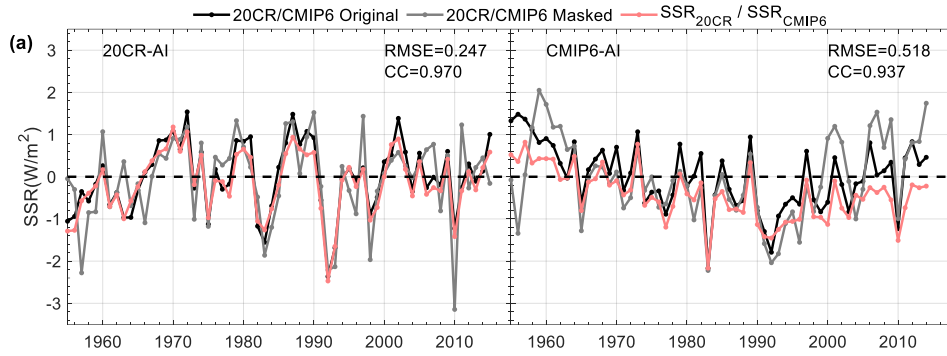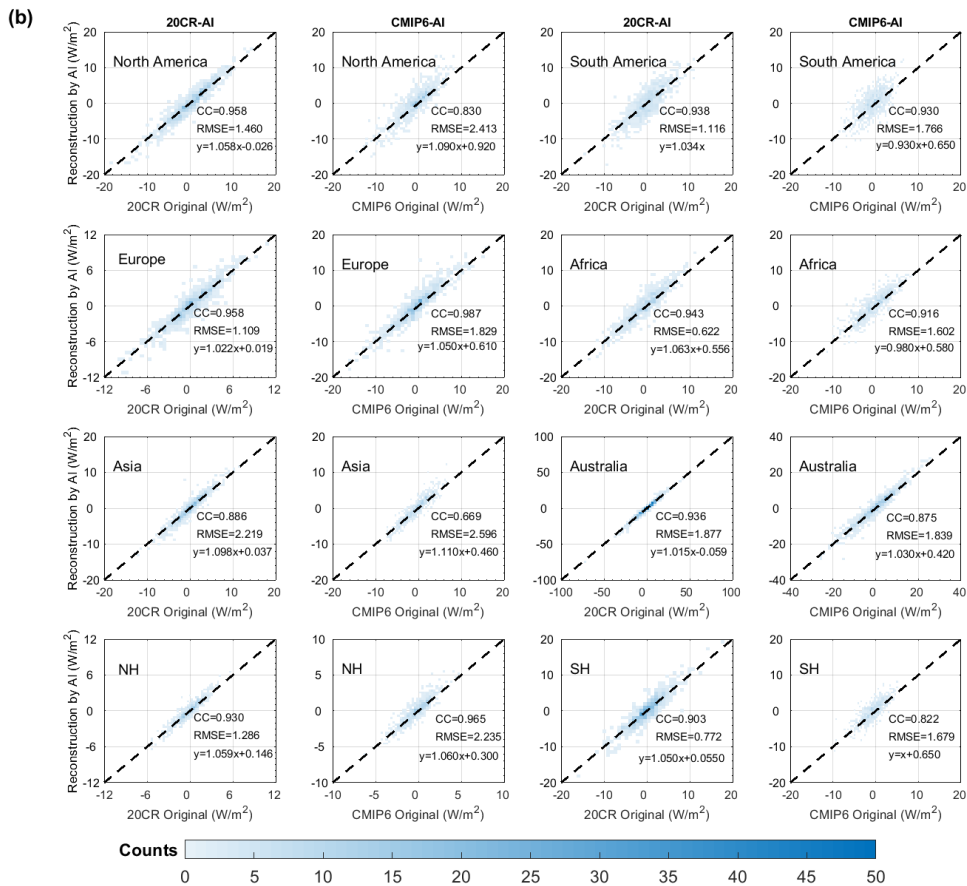
Figure 6: Reconstruction capabilities of the AI model. (a) Global land (except for Antarctica) means time-series analysis and AI model reconstruction evaluation. The red line is the SSR of the reconstruction based on the 20CR-AI /CMIP6-AI model (SSR_{20CR} /SSR_{CMIP6}); The grey line is the masked datasets with missing values of the $SSRIH_{grid}$. The solid black line is the 20CR and CMIP6 validation set (the SSR from the 1th member of 20CRv3 /CMIP6). (b) Comparisons of the SSR_{20CR} (columns 1, 3) /SSR_{CMIP6} (columns 2, 4) with the SSR from the 20CR and CMIP6 validation set. Colour bars represent counts with the same values for both. Figures also show the SSR_{20CR} (SSR_{CMIP6}) correlation coefficient (CC), root mean squared error (RMSE) and fitting equation compared to the original dataset in different regions.
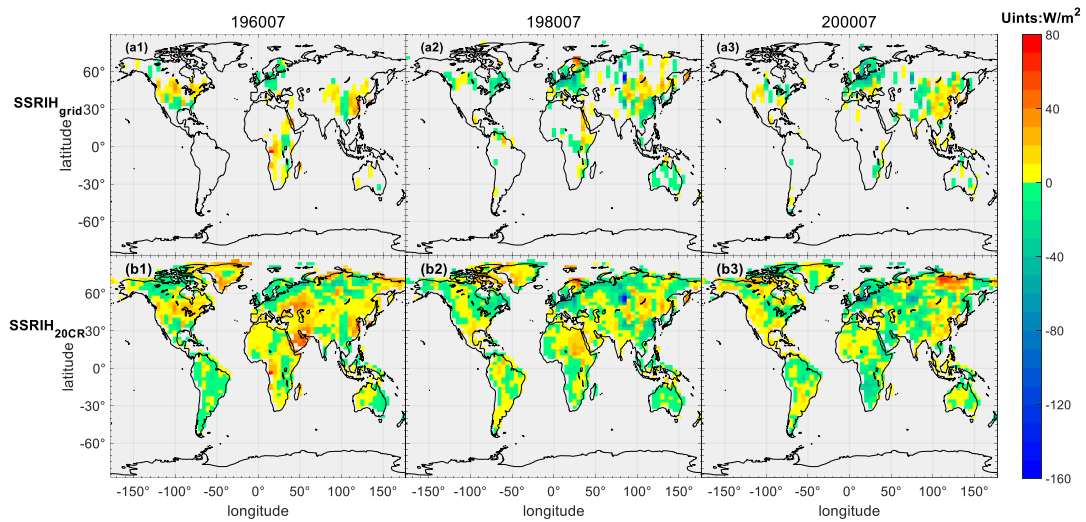
845

Figure 7: Spatial distribution of the SSRIH$_{grid}$ (a1-3) and SSRIH$_{20CR}$ (b1-3) in typical months. 1-3 is July 1960, July 1980, and July 2000, respectively.
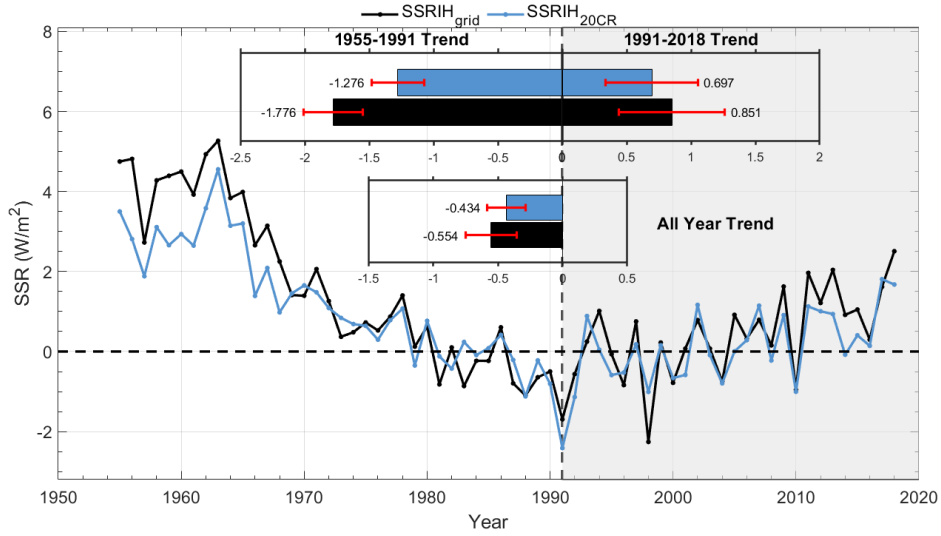
848

849 **Figure 8: Global land (except for Antarctica) annual SSR anomaly variations (relative to 1971-2000)**

850 **before/after reconstruction. The Black solid line represents the SSRIH$_{grid}$ annual anomalies. The solid blue**

851 **line represents the SSRIH$_{20CR}$ annual anomalies. The histograms represent the decadal trends of the**

852 **SSRIH$_{grid}$ /SSRIH$_{20CR}$ (unit: W/m^2 per decade) and their 95% uncertainty range from 1955 to 1991, 1991-**

853 **2018 and 1955-2018.**

854
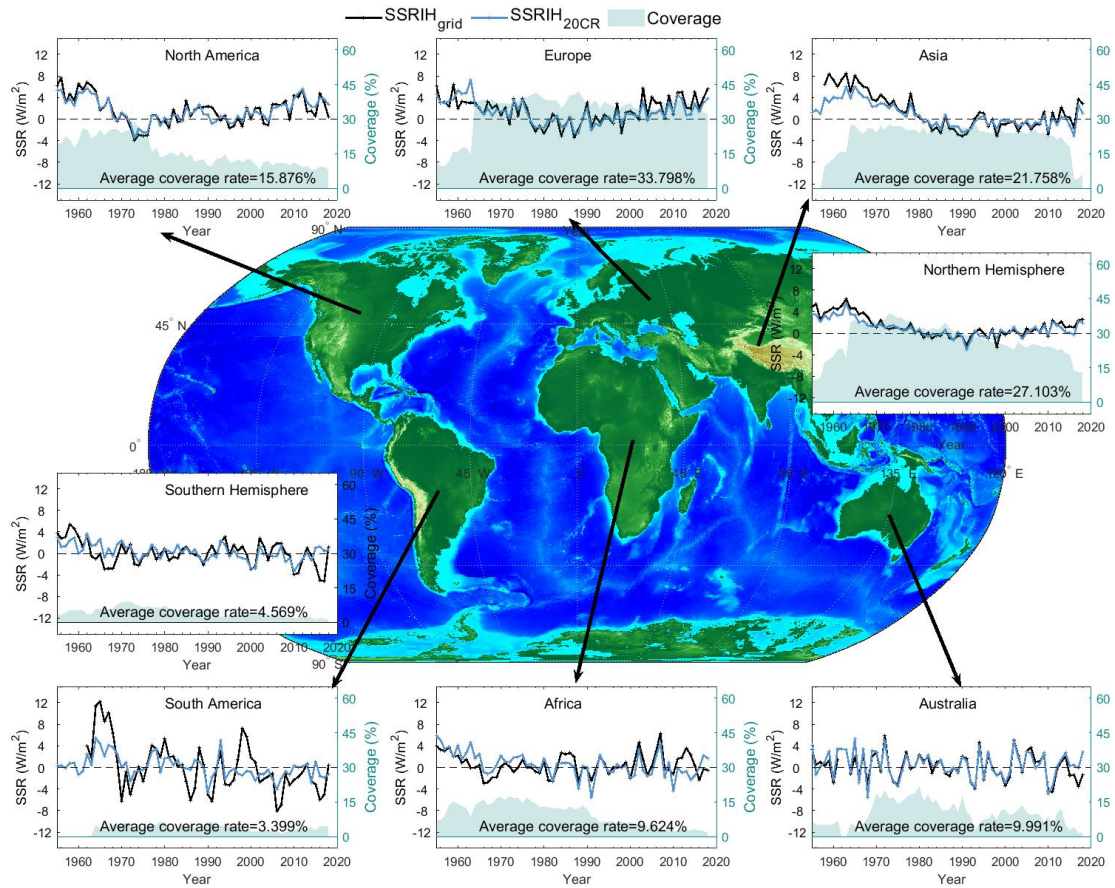
Figure 9: Same as Figure 8, but for regional annual anomaly variations. The green colour filling diagram

represents the variation in grid box coverage (before reconstruction).